Li-Ion Batteries

Introducing 4s–2p Orbital Hybridization to Stabilize Spinel Oxide Cathodes for Lithium-Ion Batteries

Gemeng Liang, Emilia Olsson, Jinshuo Zou, Zhibin Wu, Jingxi Li, Cheng-Zhang Lu, Anita M. D'Angelo, Bernt Johannessen, Lars Thomsen, Bruce Cowie, Vanessa K. Peterson, Qiong Cai, Wei Kong Pang,* and Zaiping Guo*

Abstract: Oxides composed of an oxygen framework and interstitial cations are promising cathode materials for lithium-ion batteries. However, the instability of the oxygen framework under harsh operating conditions results in fast battery capacity decay, due to the weak orbital interactions between cations and oxygen (mainly $3d$–$2p$ interaction). Here, a robust and endurable oxygen framework is created by introducing strong $4s$–$2p$ orbital hybridization into the structure using $LiNi_{0.5}Mn_{1.5}O_4$ oxide as an example. The modified oxide delivers extraordinarily stable battery performance, achieving 71.4 % capacity retention after 2000 cycles at 1 C. This work shows that an orbital-level understanding can be leveraged to engineer high structural stability of the anion oxygen framework of oxides. Moreover, the similarity of the oxygen lattice between oxide electrodes makes this approach extendable to other electrodes, with orbital-focused engineering a new avenue for the fundamental modification of battery materials.

Introduction

The next major challenge for commercial lithium-ion battery (LIB) development is their limited energy density, where cathode materials are regarded as the performance bottleneck.[1] Oxides are the most common LIB cathode materials, including layered, spinel, and polyanion types.[2] Structurally, oxide materials are composed of a metal–oxygen framework with shared oxygen ions at adjacent polyhedra and cations central in polyhedral.[2] Compared to their S-based predecessors in the 1970s, the metal–oxygen framework within oxides facilitates high oxidation state of transition metal (TM) ions, increasing the battery operating voltage and energy density.[3] The metal–oxygen framework enables lithium diffusion, and the stability of this framework underpins the stability of overall battery performance.

Interstitial cations significantly influence the framework properties through orbital interactions with lattice oxygen.[4] Here, a direct example is demonstrated by the oxygen redox reactions of Li-rich layered oxides, in which □–O–Li and □–O–□ (□ = Li vacancies) form upon lithium extraction, leaving local orphaned oxygen $2p$ orbital and causing undesirable structural degradation.[4] Another example is Mn-based oxide, in which the existence of Mn^{3+} ([Ar] $3d^4$) distorts the Mn–O framework due to the Mn $3d$ orbital degeneracy, known as Jahn–Teller distortion[5] and causing subsequent battery performance decay. These examples show that an orbital-level understanding is important in directing the modification of oxide structures, where, unfortunately, inadequate research attention has been paid till now.

Generally, cations at interstitial octahedral/tetrahedral sites in commercial cathodes belong to the $3d$ TM

[*] Dr. G. Liang, Dr. Z. Wu, J. Li, Prof. V. K. Peterson, Dr. W. K. Pang, Prof. Z. Guo
Institute for Superconducting & Electronic Materials,
University of Wollongong
Wollongong, NSW (Australia)
E-mail: wkpang@uow.edu.au
zaiping.guo@adelaide.edu.au

Dr. G. Liang, Dr. J. Zou, Prof. Z. Guo
School of Chemical Engineering & Advanced Materials,
The University of Adelaide
Adelaide (Australia)

Dr. E. Olsson, Prof. Q. Cai
Department of Chemical and Process Engineering,
University of Surrey
Guildford GU2 7XH (UK)

Dr. C.-Z. Lu
Industrial Technology Research Institute
Hsinchu (Taiwan)

Dr. A. M. D'Angelo, Dr. B. Johannessen, Dr. L. Thomsen, Dr. B. Cowie
Australian Synchrotron, Australian Nuclear Science and Technology Organization, VIC (Australia)

Prof. V. K. Peterson
Australian Centre for Neutron Scattering, Australian Nuclear Science and Technology Organization
Sydney (Australia)

Angew. Chem. Int. Ed. **2022,** *61,* e202201969 (1 of 11)

© 2022 The Authors. Angewandte Chemie International Edition published by Wiley-VCH GmbH

elements,[6] such as Mn^{3+} ([Ar] $3d^4$) and Ni^{2+} ([Ar] $3d^8$), which form TM 3d-O 2p orbital interactions in the structures. However, these interactions are insufficient to stabilize the metal–oxygen framework during delithiation/lithiation, resulting in various battery performance issues. To support the stabilization of these material structures, different dopant elements have been introduced,[7] the majority of which are n*d* elements (*n* = 3, 4, 5), such as 3*d* Cr^{3+}, 4*d* Ru^{4+}, and 5*d* Ir^{4+}. Taking commercial spinel-type $LiMn_2O_4$ cathodes as an example, doping with Cr and Ru increases battery capacity retention by 13% and 18%, respectively, after 30 cycles.[7e,f] Unfortunately, these improvements are not satisfactory enough yet due to the significant difference between energies of TM n*d* and O 2p orbitals,[8] highlighting the importance of judicious dopant selection. As informed by the molecular orbital theory and corresponding molecular orbital energy diagrams of oxides (Figure S1),[9] a σ-type molecular bonding formed by 4*s* and 2*p* orbitals exhibits a significantly reduced orbital energy, compared to that derived from 3*d* and 2*p* orbitals. The lower energy corresponds to more stable orbital interaction and lattice structure. To the best of our knowledge, tuning of such orbital interactions has not been employed as a strategy to stabilize battery cathode structures.

We turn our attention to the spinel-type $LiNi_{0.5}Mn_{1.5}O_4$ (LNMO) oxide, a promising high-energy-density cathode for LIBs with high operating voltage of 4.7 V, the practical application of which is limited by relatively poor structural stability and the decomposition of electrolytes due to high operating voltage.[10] Our search for 4*s* and 2*p* orbital interaction led us to Ge_2O_3,[11] in which Ge with a valence state of +3 has electrons in the 4*s* orbital, available for the interaction with O electrons in the 2*p* orbital. In this work, we successfully introduce this novel Ge 4*s*-O 2*p* orbital interactions into the LNMO structure for the first time, as confirmed by theoretical calculations and various cutting-edge characterization techniques, including X-ray photoelectron spectroscopy (XPS), X-ray absorption spectroscopy (XAS) and near-edge X-ray absorption fine structure (NEXAFS) spectroscopy. The metal-oxygen framework of spinel oxides is radically strengthened by this modification, allowing complete delithiation without structural disruption and two-phase reactions at high voltage, as supported by the observation in synchrotron-based X-ray powder diffraction (sXRPD) experiments. The well-maintained oxygen states and increased defect formation energy of oxygen vacancy as observed in NEXAFS and theoretical calculations, respectively, are considered the root cause of the enhancement mechanism. The modified LNMO with optimized 4*s*–2*p* orbital interaction (chemical formula of $LiNi_{0.5}Mn_{1.48}Ge_{0.02}O_4$, termed 4*s*-LNMO) exhibits extraordinarily stable battery performance at 1 C with capacity retention of 84.9% and 71.4% after 1000 and 2000 cycles, respectively, in sharp contrast to the rapid capacity decay of unmodified LNMO with only 3*d*–2*p* orbital interaction. Moreover, considering the similar oxygen lattices of spinel-type, layered-type, and lithium-rich layered-type oxides, our orbital-interaction-targeted modification strategy for metal–oxygen framework stabilization is extendable to other cathode systems. This work sheds light on the influence of orbital interactions in oxide electrode stability and points out a promising research strategy for battery researchers to design high-performance active materials.

Results and Discussion

Similar irregular-polyhedral morphological features were observed for LNMO and 4*s*-LNMO using scanning electron microscopy (SEM, Figures S2a and S2b), indicating a minor effect of Ge doping on the morphology of particles. The uniform distribution of all elements within 4*s*-LNMO was confirmed using energy-dispersive X-ray spectroscopy (EDS) elemental mapping (Figures S2c–S2h). The detailed crystal structure of 4*s*-LNMO was investigated using aberration-corrected scanning transmission electron microscopy (STEM) in high-angle annular dark-field (HAADF) mode (Figures 1a–d). Figures 1b and c show the corresponding results of the two selected regions in Figure 1a, in which only Ni, Mn, and Ge are expected and appear as small bright spots.[12] In both regions, typical diamond shapes of spinel structures are clearly identified, consistent with previous reports.[13] The spot intensity is noted to be proportional to the atomic numbers. The minor increase in the 16*d* peak intensity (Figure 1e) can be observed in the yellow region and arises from the partial replacement of Ni/Mn by Ge (Ni, $Z = 28$; Mn, $Z = 25$; Ge, $Z = 32$). Additionally, in both yellow and cyan regions, some center-filled diamonds could also be observed, which corresponds to the occupation of 16*c* sites within the spinel $Fd\bar{3}m$ structure by Ge dopants (Figures 1b, c, and d).[10a,13a] Center-filled diamonds aggregate at the particle surface with a thickness of ≈20 nm (Figure 1c), forming a "Ge-rich" region, with respect to "Ge-poor" region in inner bulk, as confirmed by the results of the sub-surface area (Figure 1d) and higher intensity ratios of $peak_{16c}/peak_{16d}$ in Figure 1f than that in Figure 1e. To conclude, the location of Ge dopants distributes across the whole particle at both 16*d* and 16*c* sites of the $Fd\bar{3}m$ structure, while segregation of 16*c*-seated Ge could be found on the particle surface.

Neutron powder diffraction (NPD) at neutron wavelengths of 1.62147(2) and 2.43853(4) Å, and laboratory X-ray powder diffraction (XRPD) data of 4*s*-LNMO were used in joint Rietveld refinement of the crystal structure, with the refinement profiles shown in Figures 1g,h, and S3, respectively. The corresponding Rietveld refinement profiles using data of LNMO are shown in Figure S4. Detailed refinement results are tabulated in Table S1. We note that powder diffraction techniques probe the average bulk information of the materials. The larger lattice parameter of 4*s*-LNMO ($a = 8.16607(9)$ Å, vs. $a = 8.1638(1)$ Å of LNMO) further reinforces the successful doping of Ge into the spinel-type structure. Figure 1i shows the planar nuclear density contour map (at $z/c = 0.5$), which is reconstructed against the observed structure factor of NPD data, alongside the schematic structure. Detailed density maps of LNMO and 4*s*-LNMO (Figures S5a and S5b, respectively) were further analyzed using line profile analysis at $x/a = 0.5$. While
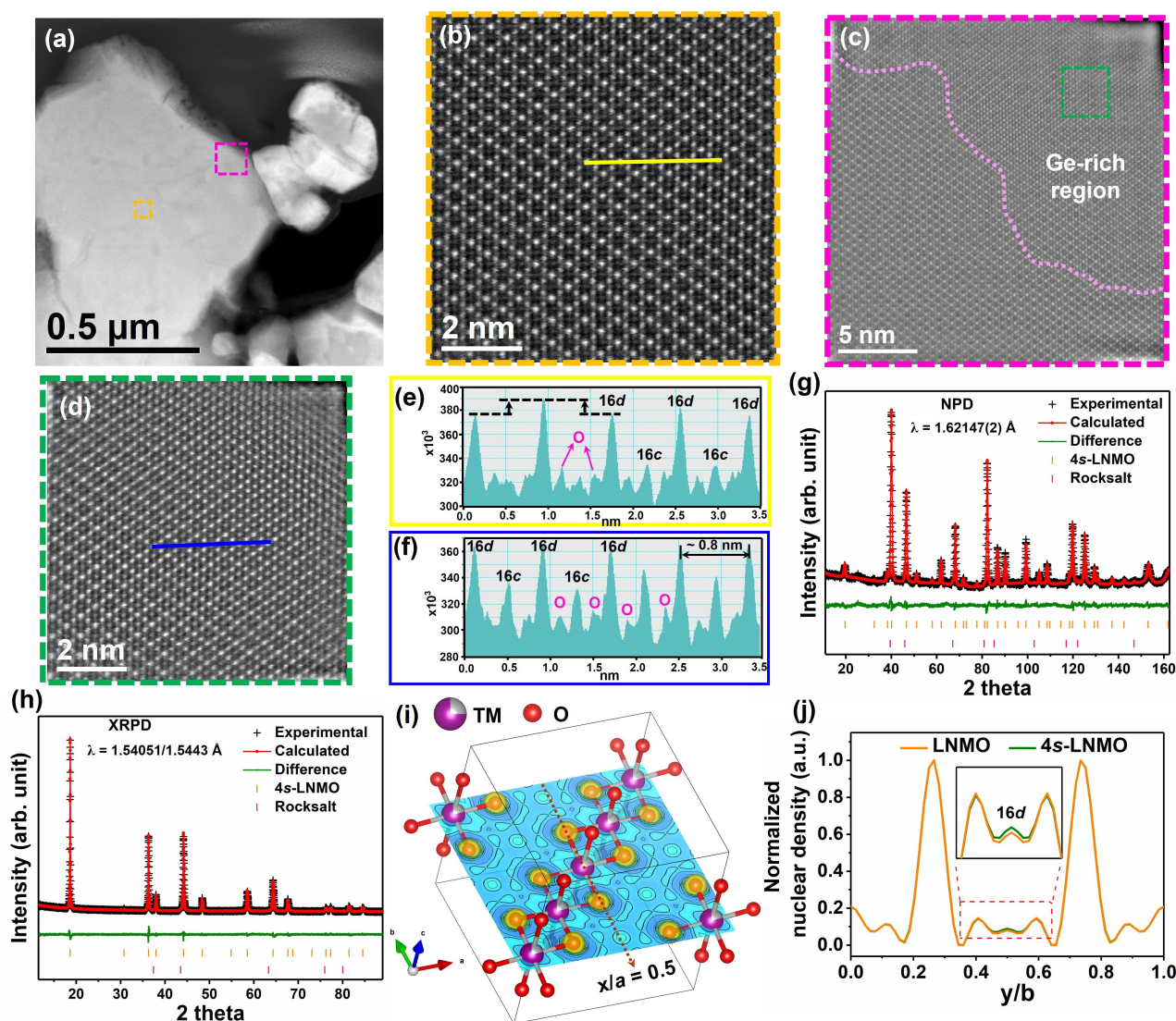
Figure 1. a) Typical HAADF STEM image of 4s-LNMO, enlargement of the yellow (b) and green (c) areas in (a); d) enlargement of the green area in (c); e) and f) line profile analysis along the yellow and blue lines in (b) and (d), respectively; joint Rietveld refinement profiles using g) NPD and h) XRPD data of 4s-LNMO with weighted profile R-factor $R_{wp} = 4.80\%$ and combined goodness of fit (GOF) = 1.44; i) nuclear density contour map of spinel LNMO with intensity shown in color from highest in yellow to lowest in blue, alongside its schematic crystal structure; j) normalized nuclear density of the line profile results of LNMO and 4s-LNMO with the inset showing the details of the boxed area.

the two profiles resemble, a noticeable increase in intensity at the 16d sites could be spotted in the inset of Figure 1j, which is related to the different neutron coherent scattering lengths of Ni (10.3 fm), Mn (-3.73 fm), and Ge (8.18 fm). These findings validate the substitution of Mn by Ge at 16d sites in the bulk sample, showing good consistency with our STEM observations.

Figures 2a and S6 show the Ge 3d and 3p XPS spectra, respectively, of 4s-LNMO and reference GeO_2, where a significant peak shift is observed in both figures, indicating the lower valence of Ge in 4s-LNMO than that in GeO_2 (Ge^{4+}). The 3d spectral peak of 4s-LNMO (Figure 2a) appears at approximately 31.5 eV, in accordance with that of Ge^{3+} ([Ar] $3d^{10}4s^1$) as per previous work.[14] XPS is surface-sensitive with a detection depth of less than 20 nm, and these results, therefore, relate to the Ge-rich region

exemplified in Figures 1c and d, indicating Ge at 16c sites with a valence of $+3$. Figure 2b shows the Ge K edge XAS data of 4s-LNMO and Ge references (GeO_2 and Ge). The edge of 4s-LNMO lies between those of GeO_2 and metallic Ge, further supporting the existence of Ge^{3+} in the structure. In transmission mode of Ge K edge measurements, the detection depth can be estimated to be 20–40 μm, reflecting the bulk average of Ge valence. The average valence state of Ge in 4s-LNMO was calculated to be approximately $+3.56$ (Figure S7), indicating the 16d-seated Ge dopants to be Ge^{4+} and the molar ratio of 44%:56% between Ge^{3+} and Ge^{4+} in spinel 4s-LNMO. Accordingly, the location/valence relationship of Ge dopants in the structure has been unveiled, with Ge^{3+} and Ge^{4+} distributing at the 16c and 16d sites, respectively.
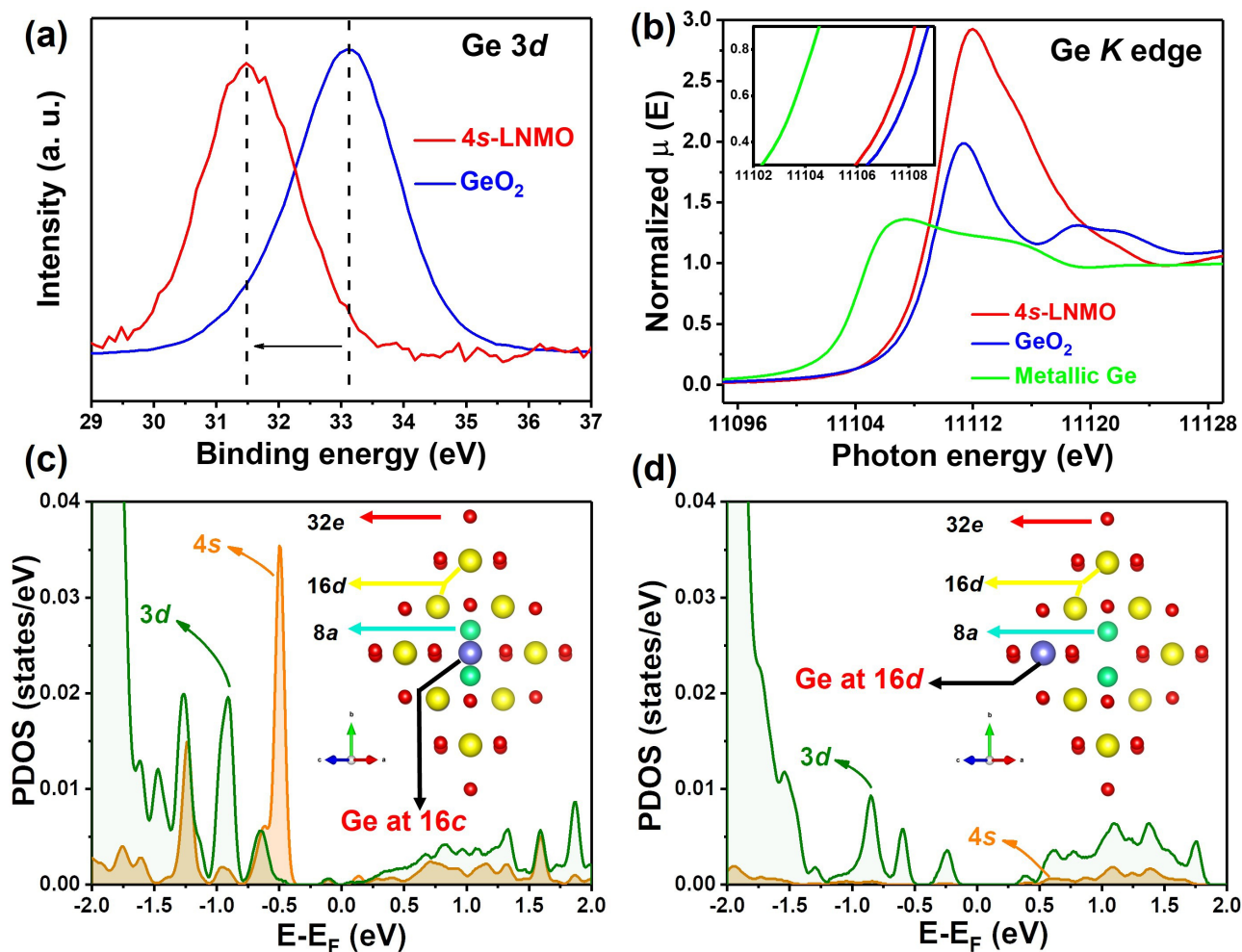
Figure 2. a) Ge 3*d* XPS data of 4*s*-LNMO and GeO$_2$; b) Ge *K* edge XAS data of 4*s*-LNMO and reference materials of GeO$_2$ and Ge. The inset corresponds to the enlargement of the normalized absorbance from 0.3 to 0.9; projected density of states (PDOS) for the spinel materials with Ge locating at c) 16*c* and d) 16*d* site, respectively. The inset in (c) and (d) is a schematic of Wyckoff sites in the spinel-type structure with *Fd3̄m* space group symmetry shown along the [101] direction.

Further details of Ge at 16*d* and 16*c* sites of the spinel-type structure were probed using density functional theory (DFT) calculations. The calculated defect formation energy (E_f) of Ge at 16*d* site ($E_f = -0.55$ eV) is significantly lower (more energetically favorable) than that at 16*c* site ($E_f = 1.16$ eV). Typically, E_f of oxide defects, such as Li vacancies in LiCoO$_2$ and anti-site defects in Na$_{2/3}$Fe$_{1/2}$Mn$_{1/2}$O$_2$, ranges from 3 to 4 eV.[15] Our calculated E_f for Ge indicates that both 16*c* and 16*d* sites are favorable for Ge doping, with 16*d* sites more likely to be occupied at equilibrium. The calculated projected density of states (PDOS) of Ge at 16*c* and 16*d* sites in LNMO (Figures 2c and d) are significantly different. For Ge at 16*c* site (Figure 2c), there is a large contribution from the Ge *s*-states around the Fermi level, which is not observed for the 16*d* site (Figure 2d). This further supports that Ge^{3+} ([Ar] 3d^{10}4s^1) and Ge^{4+} ([Ar] 3d^{10}) reside at 16*c* and 16*d* sites, respectively. Although a significant difference in the Bader charges of Ge (q_{Ge}) at 16*c* ($q_{Ge} = 2.29$ e) and 16*d* ($q_{Ge} = 2.36$ e) sites is not observed from the simulations, a calculation for GeO$_2$ ($q_{Ge} = 2.40$ e)

suggests that q_{Ge} of Ge at the 16*d* site is closer to the common +4 valence state than Ge at the 16*c* site, consistent with our previous observations. Calculated Bader charges are summarized in Table S2. To conclude, these calculations probe the location/valence/function relationships of Ge dopants within the LNMO structure, revealing that Ge at 16*d* sites owns a valence state of +4 ([Ar] 3d^{10}) and results in 3*d*–2*p* orbital hybridization. In contrast, Ge at 16*c* sites uniquely shows a valence state of +3 ([Ar] 3d^{10}4s^1) and contributes to novel 4*s*–2*p* orbital hybridization. The contribution of 3*d*–2*p* orbital hybridization generated by Ge^{4+} dopants to improve the structural stability could be summarized in two aspects. Firstly, it could help suppress the notorious cooperative Jahn–Teller distortion and reduce the parasitic Mn dissolution, thus maintaining the spinel structural integrity.[6a] Secondly, the Ge–O bond (Ge 3*d*-O 2*p* orbital interaction) has a higher bond dissociation energy (662 kJ mol^{-1}) than the Mn–O bond dissociation energy (402 kJ mol^{-1}),[16] significantly strengthening the metal-oxygen framework. On the other hand, the changes in the

structure brought by this 16*d* substitution could be trivial due to the same valence state (+4), same ionic radius (0.53 Å), and similar interaction with oxygen orbitals (3*d*–2*p* hybridization) of Ge^{4+} and Mn^{4+} ions.[17]

Comparison of the electrochemical performance of modified LNMO with different Ge concentrations has been made in Figure S8. It is obvious that the dopant concentration plays a vital role in the electrochemical performance of the active material, where modified LNMO with 2% Ge ($LiNi_{0.5}Mn_{1.48}Ge_{0.02}O_4$, i.e. 4*s*-LNMO) delivers the highest battery capacity alongside superior cycling stability. Reduced Ge concentration in the structure corresponds to insufficient 4*s*–2*p* orbital interaction in the spinel structure, thus failing to ensure a robust metal-oxygen framework during charge/discharge. Meanwhile, excess Ge doping in the spinel could lead to inferior battery performance, probably because excess Ge^{3+} dopants occupy the 16*c* sites of $Fd\bar{3}m$ structure and sacrifice the active Li sites in the spinel. We focus our comparison on the pristine LNMO and high-performance 4*s*-LNMO. Cyclic voltammogram (CV) results at different sweep rates reveal similar electrochemical behavior of LNMO and 4*s*-LNMO (Figures 3a and b).

Peaks at approximately 4.0 V arise from Mn^{3+}/Mn^{4+}, while peaks at about 4.7 V correspond to the Ni redox couples, with lower (peak 1 and 4) and higher (peak 2 and 3) peaks corresponding to Ni^{2+}/Ni^{3+} and Ni^{3+}/Ni^{4+} couples, respectively, as consistent with previous work.[7a, 18] The linear relationship between peak current i_p and the square root of the sweep rate ($v^{1/2}$) of the Ni-redox-related peaks (Figures 3c and d) confirms the diffusion-controlled behavior of the spinel electrode.[18b,c] The lithium diffusion coefficient (D_{Li}) of each peak could be calculated according to the Randles–Sevcik equation,[18b,c] with more calculation details found in the Experimental Methods. The calculated D_{Li} of each peak is shown in Figures 3c and d, revealing that 4*s*-LNMO owns faster lithium transportation (about 70% higher for peak 1–3 and 136% higher for peak 4) than LNMO.

Figure 3e compares the cycling performance of LNMO and 4*s*-LNMO at 1 C (1 C = 147 mA g^{-1}). Obviously, initial battery capacity of 133.4 mAh g^{-1} is observed for 4*s*-LNMO, much higher than those for LNMO (114.9 mAh g^{-1}) and other modified LNMOs in previous reports (Figure S9a), demonstrating the superiority and importance of 4*s*–2*p*
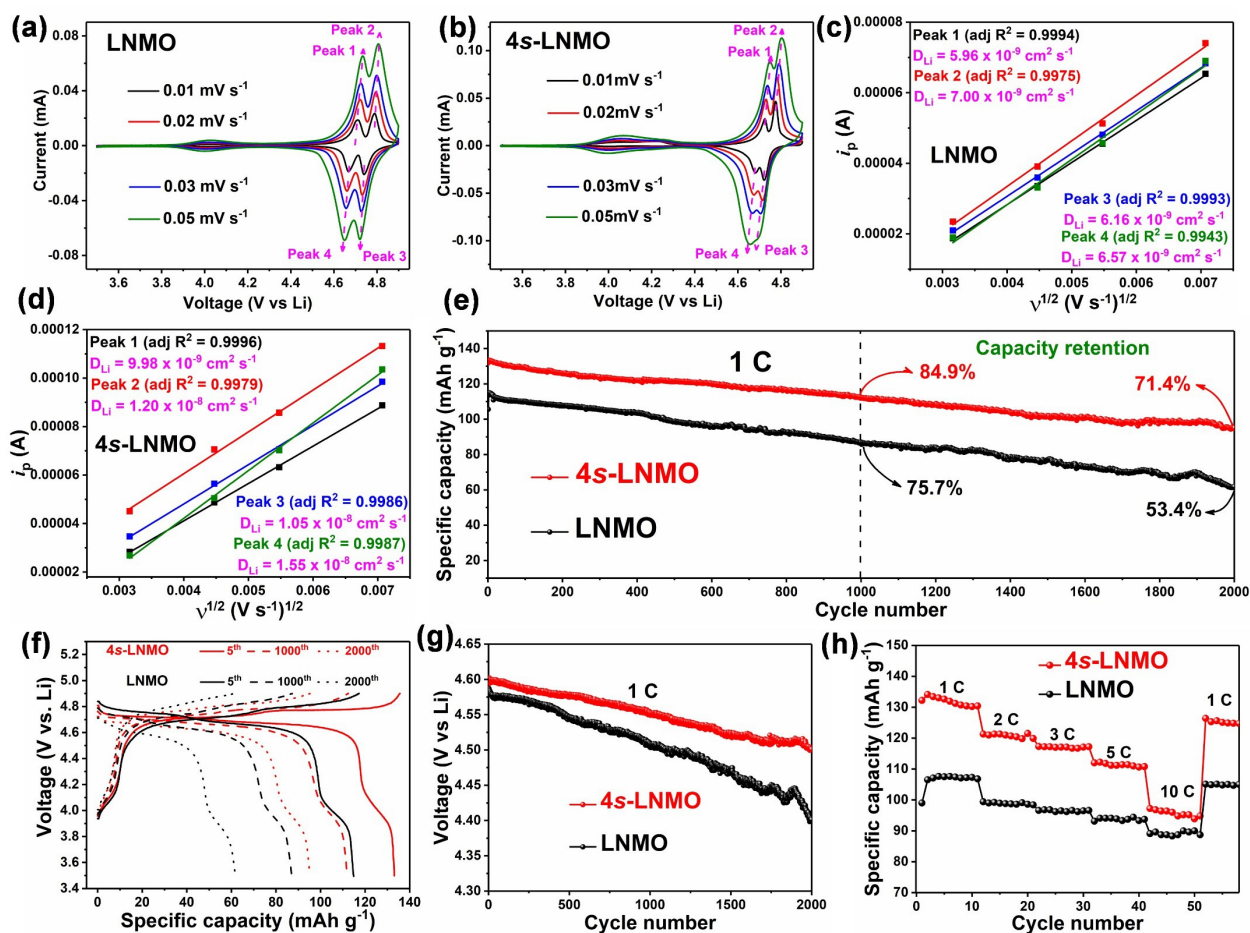

Figure 3. CV curves of a) LNMO and b) 4*s*-LNMO at different scanning rates; corresponding linear-fitted peak current vs. square root of the scan rate for c) LNMO and d) 4*s*-LNMO; e) cycling performance of LNMO and 4*s*-LNMO at 1 C and f) corresponding charge/discharge curves of both samples at the 5th, 1000th, and 2000th cycles; g) average discharge voltage of LNMO and 4*s*-LNMO at 1 C; h) rate capability of LNMO and 4*s*-LNMO.

orbital hybridization in our 4s-LNMO. Meanwhile, 4s-LNMO delivers a high reversible capacity of 113.2 mAh g⁻¹ after 1000 cycles, corresponding to high capacity retention up to 84.9%, significantly better than LNMO (86.9 mAh g⁻¹, capacity retention of 75.7%). Moreover, 4s-LNMO retains 71.4% of its initial capacity after 2000 long cycles, in sharp contrast to LNMO (53.4%). Figure S9b further highlights the superior cycling stability of 4s-LNMO over other LNMO materials. Corresponding electrochemical curves at the 5th, 1000th, and 2000th cycles of the two samples are shown in Figure 3f, in which three voltage plateaus during charge/discharge are observed, in accordance with CV observations. Severe voltage polarization is observed for LNMO as the cycle number increases, in contrast to the relatively minor polarization experienced by 4s-LNMO. Figure 3g shows the average discharge voltage of LNMO and 4s-LNMO, where LNMO suffers a rapid decay from 4.58 to 4.39 V during 2000 cycles, and 4s-LNMO decays from 4.60 to only 4.51 V over this period. In summary, the stable battery performance, significantly reduced voltage polarization, and high output voltage of 4s-LNMO during cycling confirm a robust metal-oxygen framework with excellent structural stability, highlighting the benefits of 4s–2p orbital hybridization.

Energy densities of LNMO and 4s-LNMO at 1 C are compared in Figure S10. As expected, 4s-LNMO delivers an energy density of 613.5 Wh kg⁻¹, much larger than that of the undoped LNMO (526.3 Wh kg⁻¹). Additionally, after 2000 cycles, high energy density of 428.5 Wh kg⁻¹ is maintained by 4s-LNMO, compared to the severe energy decay experienced by LNMO (269.7 Wh kg⁻¹). Electrochemical testing of LNMO and 4s-LNMO at lower current density (0.1 C) are shown in Figure S11. As expected, 4s-LNMO could deliver large reversible battery capacity up to 143 mAh g⁻¹ at 0.1 C (Figure S11a), much higher than that of LNMO (131 mAh g⁻¹), and retain 95.8% of its initial capacity after 150 cycles, in sharp contrast to LNMO (78.2%). Meanwhile, significant voltage polarization, similar to that in Figure 3f, occurs in LNMO as the cycle number increases, which is avoided by 4s-LNMO (Figure S11b), again confirming the necessity and success of our proposed 4s–2p orbital interaction. Figure 3h compares the rate capability of LNMO and 4s-LNMO, in which a superior rate performance is observed for 4s-LNMO, delivering specific capacities of 121.3, 117.2, 111.8, and 97.2 mAh g⁻¹ at 2, 3, 5, 10 C, respectively, in comparison to the equivalents of LNMO (98.9, 96.2, 94.1, and 88.3 mAh g⁻¹, respectively).

Post-mortem NEXAFS analysis of LNMO and 4s-LNMO electrodes (Figure 4) was carried out in total-electron-yield mode, with detection depth of approximately 5 nm. Figures 4a, b, and S12 show O K edge NEXAFS spectra, which originate from the 1s–2p dipole transition of oxygen.[19] Peaks A and B in the pre-edge zone (528–534 eV) arise from the hybridization between O 2p and localized Ni/Mn 3d orbitals. The former corresponds to the combination of spin-down t_{2g} and spin-up e_g states, while the latter relates to spin-down e_g states.[19] Peaks C and D are associated with the hybridization of O 2p and metal 4s and 4p orbitals, respectively.[19b]

O K edge spectra of LNMO and 4s-LNMO at open-circuit voltage (OCV) (Figure S12a) appear similar, except for the apparent increase at peak C, further confirming the existence of the Ge-induced metal 4s-O 2p orbital hybridization in 4s-LNMO. All peaks evolve synchronously with the states of charge of the electrodes. At fully charged states, the spectra of both samples demonstrate similar evolution, with decreasing intensity observed for peaks A and B (Figure S12b). However, a significant change at peak C is spotted in the unmodified LNMO (Figure 4a), where the shape of peak C maintains well in 4s-LNMO (Figure 4b), confirming the superior stability of 4s–2p orbital hybridization at the presence of Ge³⁺ ([Ar] $3d^{10}4s^1$). The difference between LNMO and 4s-LNMO becomes more prominent at fully discharged states. In the pre-edge zone, peak A is barely observed in discharged LNMO. In contrast, peaks A and B almost recover in 4s-LNMO after discharge. The decay of peak A in LNMO indicates the loss of spin-down t_{2g} contribution, implying a significant reduction of Mn content on the surface, the occurrence of Mn dissolution, and the irreversible oxygen change. Moreover, impressively, peak C in 4s-LNMO is well maintained together with the distinguishable peak D, again evidencing a significant contribution of the 4s–2p orbital interaction to oxygen stability.

Peak E has been widely reported as the fingerprint of carbonate species, critical components of the cathode-electrolyte interphase (CEI). Excessive CEI on the particle surface usually results in sluggish reaction kinetics.[13b] It is evident that LNMO suffers thick and continuous CEI growth on the particle surface during cycling, while 4s-LNMO is free of this hazardous issue during cycling. As informed by Li et al.,[20] the well-stabilized surface oxygen in the spinel structure could relieve the electrolyte decomposition at the electrode/electrolyte interphase. Therefore, the enhanced oxygen stability at the particle surface induced by the 4s–2p bond contributes to a stable and thin CEI in 4s-LNMO. Meanwhile, Ge³⁺ locates at partial 16c sites of 4s-LNMO, forming local "rock-salt" phase within the structure, in which the 16c-seated Ge³⁺ act as structural pillars to prevent the structural collapse at highly delithiated states, therefore transforming hazardous two-phase reaction into preferable solid-solution reactions (Figure 5). To conclude, strongly anchored surface oxygen by intense 4s–2p orbital interaction and the formation of rock-salt structure by 16c-seated Ge³⁺ contributes to the superior cycling stability of 4s-LNMO in Figure 3.

Figures 4c and d show Mn L edge spectra of LNMO and 4s-LNMO, respectively, before cycling and after 500 and 1000 cycles. Unsurprisingly, the spectra of cycled LNMO electrodes show characteristic peaks of Mn³⁺ and Mn²⁺ species, which are associated with the structural distortion as a result of Jahn–Teller effects and the Mn disproportional reaction that happened in the Mn-based spinel,[13b, 21] supporting the observation of reduced Mn content in O K edge results. Further, these undesirable reactions intensified with cycling, as indicated by the increase in peak intensity, further degrading the battery performance. In contrast, the spectra of 4s-LNMO remain relatively unchanged even after
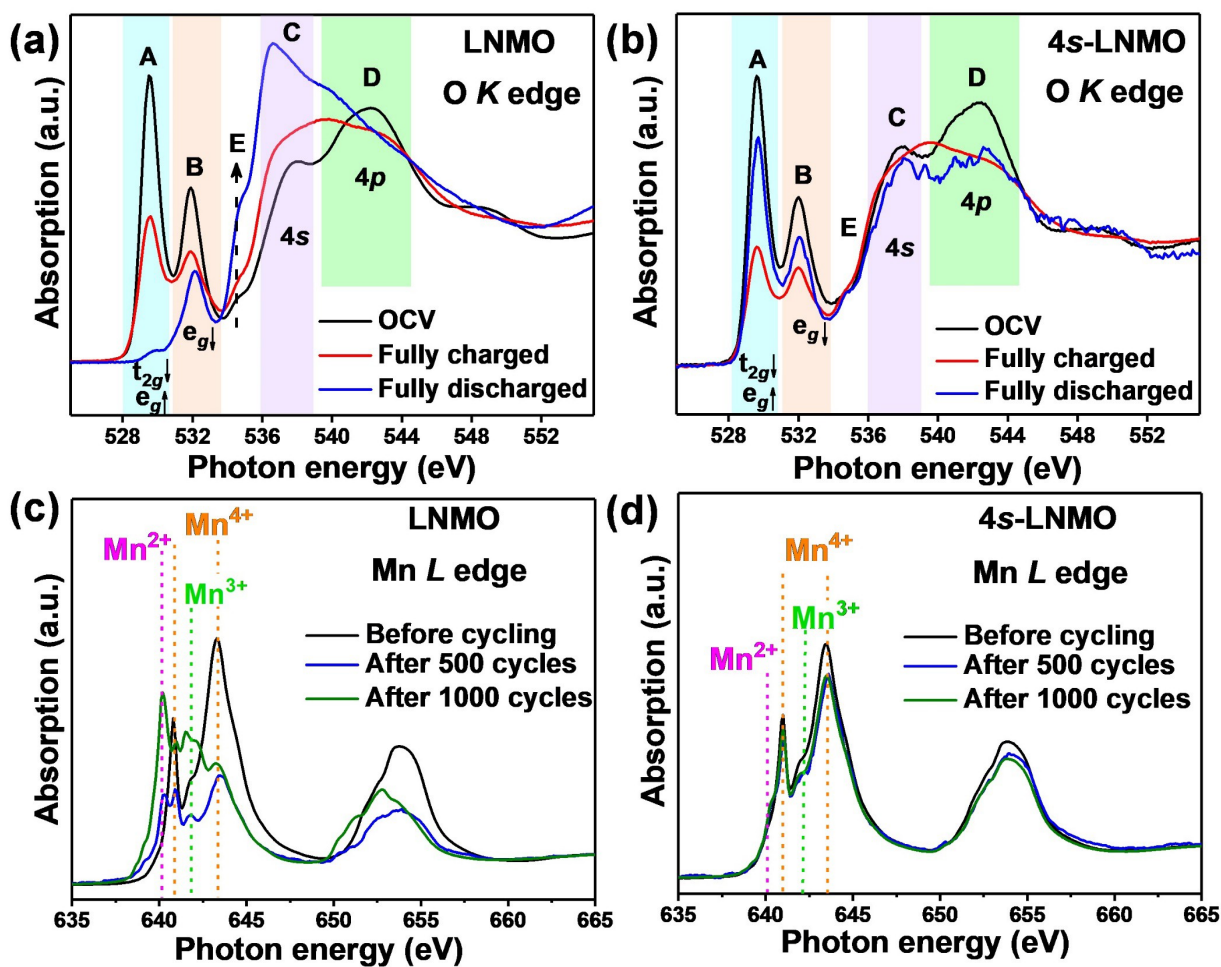
Figure 4. O K edge NEXAFS spectra of a) LNMO and b) 4s-LNMO at OCV, fully-charged and fully-discharged states; Mn L edge NEXAFS spectra of c) LNMO and d) 4s-LNMO before cycling and after 500 and 1000 cycles.

1000 cycles, with only a very minor Mn^{3+} feature and no noticeable Mn^{2+} species. The reason for this significant improvement could be ascribed to the enhanced stability of the metal-oxygen framework by $4s–2p$ interaction, remarkably overcoming the structural strains induced during repeated lithium insertion/extraction.

In operando sXRPD was used to investigate the phase and structural evolution of LNMO and 4s-LNMO during charge/discharge. The corresponding diffraction data are displayed as a contour plot in Figures 5 and S13, alongside corresponding electrochemical curves. We focus on the most intense 111 reflection in the following discussion.[10b]

From OCV to ≈4.7 V, the 111 reflection of LNMO (Figure 5a) migrates gradually to higher 2θ, corresponding to its lattice-shrinkage as a result of lithium extraction and indicating a solid-solution reaction regime within the particles. From ≈4.7 to 4.9 V, the parental reflection shows an intensity drop without a new reflection being found. On discharge, a new reflection at around 8.53° suddenly appears, which can be indexed to the 111 reflection of the rock-salt-type $Ni_{0.25}Mn_{0.75}O_2$ (NMO) phase.[22] The intensity of NMO 111 reflection keeps increasing at the beginning of

discharge, and its asymmetric behavior during cycling reveals undesirable hysteresis in the structural evolution of LNMO.[10b,23] It is known that the formation of rock-salt NMO involves the collapse of the oxygen framework and synchronous cation rearrangement, which are unfortunately not fully reversible and could result in the loss of active material.[12] When discharged to 4.6 V, the NMO reflection disappears, and the intensity of LNMO 111 reflection resumes. The 111 reflection shifts to low angles during discharge as the lithium is inserted back to the framework. Notably, a weak reflection could be found at around 8.37° after charging to ≈4.7 V and disappears at ≈4.45 V during subsequent discharge. The weak reflection could be attributed to the "incompletely-active content" in the electrode material and probably resulted from the weak contact between different battery contents (cathodes, separator, anode, etc.) at the window for X-ray to penetrate.

Unlike LNMO, 4s-LNMO shows a continuous peak evolution over the electrochemical testing (Figure 5b). Obviously, Ge doping has significantly changed the mechanistic behavior of the LNMO. The hazardous two-phase reaction at highly-charged states is well suppressed, thus
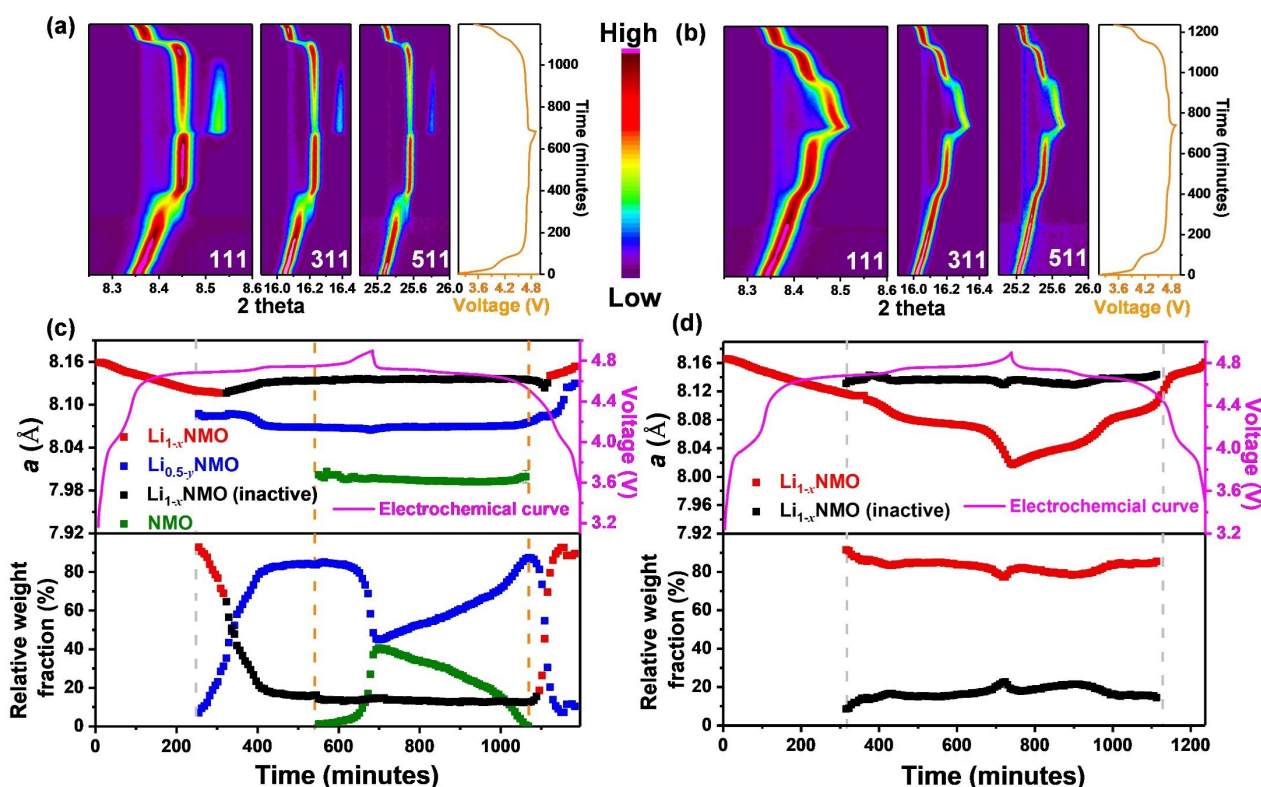
Figure 5. In operando sXRPD data in selected 2-theta regions shown as a contour map with intensity in color, corresponding to 111, 311, 511 reflections of the spinel, respectively, for a) LNMO and b) 4s-LNMO at the 1st cycle, along with the corresponding electrochemical data; evolution of lattice parameters and phase compositions, which is obtained from the sequential Rietveld refinements using in operando sXRPD data, of c) LNMO and d) 4s-LNMO at the 1st cycle, alongside their corresponding electrochemical data.

contributing to the superior cycle stability shown in Figure 3. Meanwhile, the purely single-phase or solid-solution response and the disappearance of NMO 111 reflection in 4s-LNMO reveal significantly enhanced stability of the metal-oxygen framework, which is achieved by the 4s–2p orbital hybridization, showing good agreement with the NEXAFS observations.

Further investigation into both samples at the 50th cycle was carried out, with the results shown in Figures S13a and S13b. As expected, LNMO shows noticeable structural degradation in the extended cycle. The non-continuous structural evolution and drastic two-phase reaction at highly delithiated states further aggravate the frangibility of the metal-oxygen framework. Encouragingly, a continuous and mild peak evolution with no detectable NMO 111 reflection could still be observed for 4s-LNMO at the 50th cycle, highlighting its strengthened oxygen framework and confirming the success of introducing 4s–2p interaction into the material structure.

Results of sequential Rietveld refinements using the sXRPD data are shown in Figures 5c, d, S13c, and S13d, with a typical refinement profile shown in Figure S14, in which all reflections are indexed to the spinel active material. During initial lithium extraction, the lattice parameter of $Li_{1-x}NMO$ in Figure 5c decreases from the initial 8.159(1) to 8.120(1) Å before the formation of $Li_{0.5-y}Ni_{0.5}Mn_{1.5}O_4$ ($Li_{0.5-y}NMO$, 8.07(1) Å) in a two-phase

reaction. However, it is noted that ≈15% of the $Li_{1-x}NMO$ remains as "incompletely-active content" until ≈4.45 V in discharge. $Li_{0.5-y}NMO$ turned into NMO (7.99(1) Å) via a second two-phase reaction at a higher voltage, and reversed reaction happens at about 4.5 V during discharge. At the end of discharge, the $Li_{0.5-y}NMO$ does not fully convert back to $Li_{1-x}NMO$, and 10.4(1) wt% remains, revealing the obvious irreversible structural changes of unmodified LNMO during cycling.

4s-LNMO exhibits a monotonous decrease/increase during charge/discharge (Figure 5d), respectively, indicating a robust metal–oxygen framework that endures the harsh delithiated state and tolerates the lattice strain and distortion caused by the lithium extraction/insertion across the electrochemical reaction. Moreover, the lattice parameters of 4s-LNMO before and after testing are almost identical (around 8.16 Å), confirming the fully reversible reaction (lithium transportation) within the electrode material. Moreover, 4s-LNMO also shows a smaller maximal lattice change (1.82(1)%) than the pristine LNMO (2.01(1)%), revealing the origin of the superior cycling stability of 4s-LNMO (Figure 3). Similar conclusions are found at the 50th cycle of both samples (Figures S13c and S13d), again confirming the success of the 4s–2p orbital interaction in stabilizing the oxygen framework.

To further understand the stabilization of the oxygen framework in spinel-type oxides, the oxygen vacancy for-

mation energy ($E_{f(vac)}$) was calculated in LNMO with different Ge locations (Figure 6a). The full range of $E_{f(vac)}$ in LNMO is 1.65–2.27 eV (Figure 6b), in which creating an oxygen vacancy next to two Mn, one Ni, and one Li in LNMO (Figure 6a) results in the lowest defect formation energy of 1.65 eV. It is worth noting that all the oxygen vacancy sites in LNMO have relatively low formation energies, indicating that the oxygen vacancy content in LNMO would be significant at equilibrium conditions, as shown in Table S1. Hence, the calculated $E_{f(vac)}$ values above 2.27 eV in modified LNMO indicate that the oxygen frame-

work is stabilized. To assess this further, we calculated the $E_{f(vac)}$ for an oxygen vacancy next to and 10 Å from a Ge site, by removing an oxygen from the structure. For an oxygen vacancy next to Ge at 16*d* site, $E_{f(vac)}$ increases to 2.52 eV (Figure 6b), whereas $E_{f(vac)}$ for an oxygen vacancy next to Ge at 16*c* site shows an even higher increase to 3.39 eV (Figure 6b). Moreover, an oxygen vacancy formation energy of 2.56 eV vs. 1.92 eV is found at 10 Å away from Ge at 16*c* and 16*d* site, respectively, revealing that Ge at the 16*c* site induces a more long-range effect on the stabilization of oxygen lattice. Hence, it can be concluded
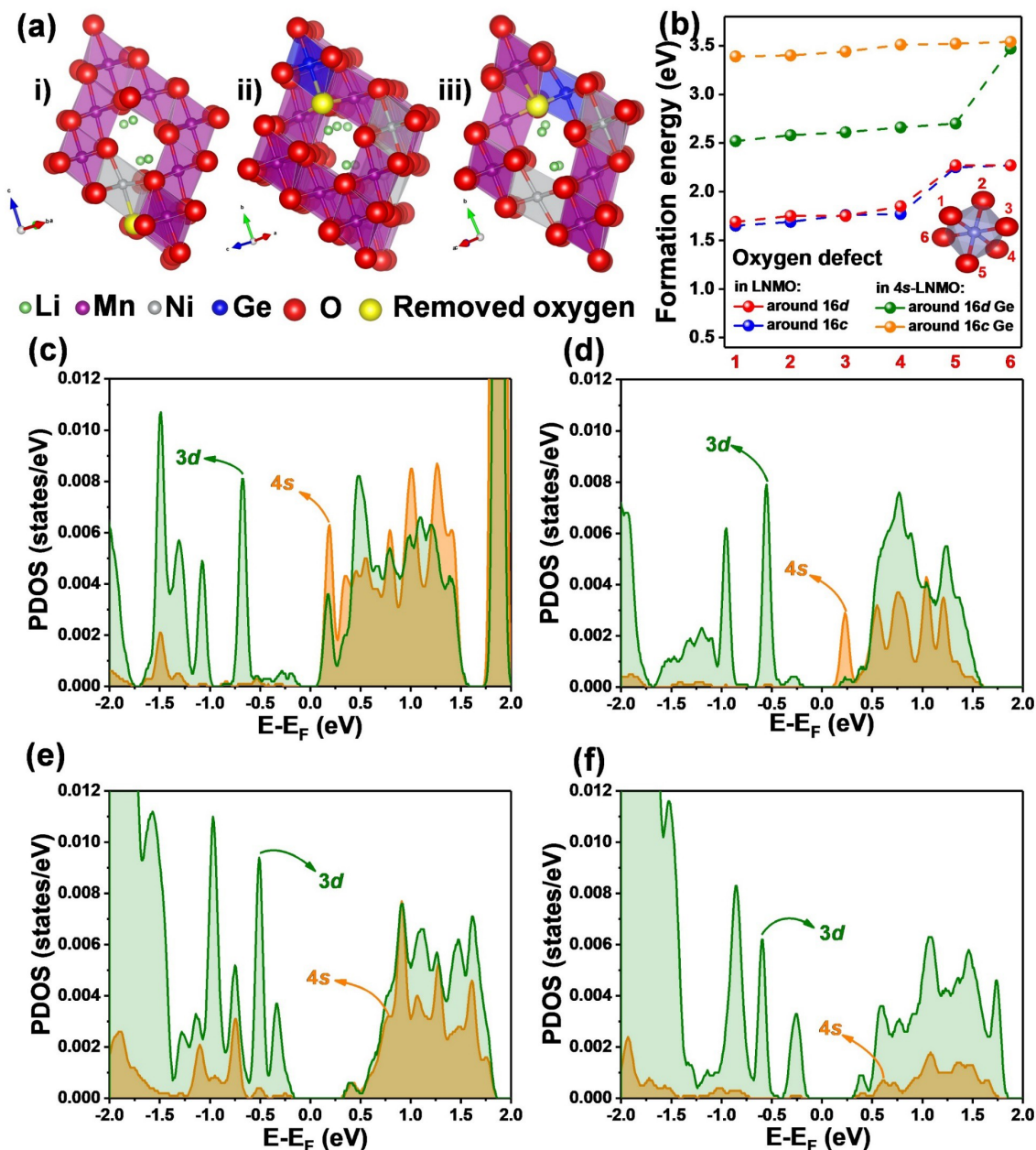

Figure 6. a) Schematic of crystal structures used in $E_{f(vac)}$ calculations for i) LNMO and modified LNMO with Ge at ii) 16*c* sites and iii) 16*d* sites; b) corresponding calculated formation energies of oxygen defects at different parts of the crystal structure, the inset schematically shows the six oxygen sites in an octahedron (dashed lines are guides to the eye); PDOS calculated for structures containing an oxygen vacancy c) next to Ge at a 16*c* site, d) 10 Å away from Ge at a 16*c* site, e) next to Ge at a 16*d* site f) 10 Å away from Ge at a 16*d* site.

that the Ge 4s-O 2p orbital hybridization indeed stabilizes the oxygen framework of LNMO. The impact of an oxygen vacancy on the electronic structure of the spinel materials was also investigated, where significant differences between modified LNMO systems with Ge locating at 16c and 16d sites, respectively, were observed (Figures 6c–f). The observed Ge s state remains in the modified LNMO with 16c-located Ge (Figures 6c and d), while it is hardly observed in 16d-located Ge (Figures 6e and f). The simulation results indicate that Ge at the 16c site stabilizes the oxygen framework of the spinel structure by increasing the $E_{f(vac)}$ for both neighboring and distant oxygens, with the favorable 4s states as shown from the experimental measurements.

Conclusion

As the most popular and promising cathode materials for LIBs, oxides have gained enormous research attention in recent decades. To realize their full battery performance at high voltage, an oxygen lattice with high stability is undoubtedly the key, where the interactions between cations and oxygen within the structure play a vital role. Except for the charge-carrier Li^+, 3d transition metals such as Ni, Mn, and Co, have been the most common cations in the oxide electrodes, forming 3d–2p orbital interaction with oxygen. As these bonds are unfortunately not strong enough to ensure a robust oxygen framework, various dopants, dominantly nd ($n = 3$, 4, 5) elements, have been introduced into the oxide structures with limited performance improvements. Here, we demonstrate a detailed orbital-level understanding of the representative high-voltage LNMO oxides and propose a novel and efficient orbital-focused modification that strengthens the oxygen lattice by introducing intense Ge 4s–O 2p orbital hybridization. Consequently, the LNMO material with 4s–2p orbital hybridization exhibits extraordinarily durable battery performance, maintaining 84.9% and 71.4% of its initial capacity after 1000 and 2000 cycles, respectively, at 1 C. Importantly, our orbital hybridization approach is extendable to other oxide electrode materials more generally, which benefits from the similarity of the oxygen lattice between oxides. This work opens new opportunities to boost the performance of oxide electrodes through orbital interaction modification, which is expected to accelerate the development of next-generation high-energy-density LIBs.

Conflict of Interest

The authors declare no conflict of interest.

Data Availability Statement

The data that support the findings of this study are available from the corresponding author upon reasonable request.

[1] a) T. Liu, L. Yu, J. Liu, J. Lu, X. Bi, A. Dai, M. Li, M. Li, Z. Hu, L. Ma, D. Luo, J. Zheng, T. Wu, Y. Ren, J. Wen, F. Pan, K. Amine, *Nat. Energy* **2021**, *6*, 277–286; b) F. Duffner, N. Kronemeyer, J. Tübke, J. Leker, M. Winter, R. Schmuch, *Nat. Energy* **2021**, *6*, 123–134.

[2] A. Manthiram, *Nat. Commun.* **2020**, *11*, 1550.

[3] A. Manthiram, J. B. Goodenough, *Nat. Energy* **2021**, *6*, 323–323.

[4] a) C. Liao, *eTransportation* **2020**, *5*, 100068; b) J. Zhang, F. Cheng, S. Chou, J. Wang, L. Gu, H. Wang, H. Yoshikawa, Y. Lu, J. Chen, *Adv. Mater.* **2019**, *31*, 1901808.

[5] M. Sturge, *Solid State Phys.* **1968**, *20*, 91–211.

[6] a) C. Zuo, Z. Hu, R. Qi, J. Liu, Z. Li, J. Lu, C. Dong, K. Yang, W. Huang, C. Chen, Z. Song, S. Song, Y. Yu, J. Zheng, F. Pan, *Adv. Energy Mater.* **2020**, *10*, 2000363; b) L. Yang, X. Li, J. Liu, S. Xiong, X. Ma, P. Liu, J. Bai, W. Xu, Y. Tang, Y. Y. Hu, M. Liu, H. Chen, *J. Am. Chem. Soc.* **2019**, *141*, 6680–6689.

[7] a) G. Liang, V. K. Peterson, K. W. See, Z. Guo, W. K. Pang, *J. Mater. Chem. A* **2020**, *8*, 15373–15398; b) M.-C. Yang, B. Xu, J.-H. Cheng, C.-J. Pan, B.-J. Hwang, Y. S. Meng, *Chem. Mater.* **2011**, *23*, 2832–2841; c) P. K. Nayak, E. M. Erickson, F. Schipper, T. R. Penki, N. Munichandraiah, P. Adelhelm, H. Sclar, F. Amalraj, B. Markovsky, D. Aurbach, *Adv. Energy Mater.* **2018**, *8*, 1702397; d) X. Zhang, Y. Qiao, S. Guo, K. Jiang, S. Xu, H. Xu, P. Wang, P. He, H. Zhou, *Adv. Mater.* **2019**, *31*, 1807770; e) G. Wang, D. Bradhurst, H. Liu, S. Dou, *Solid State Ionics* **1999**, *120*, 95–101; f) M. Reddy, S. S. Manoharan, J. John, B. Singh, G. S. Rao, B. Chowdari, *J. Electrochem. Soc.* **2009**, *156*, A652.

[8] H. B. Gray, *Electrons and Chemical Bonding*, Benjamin, New York, **1965**.

[9] a) M. Okubo, A. Yamada, *ACS Appl. Mater. Interfaces* **2017**, *9*, 36463–36472; b) K. Pierloot, *Mol. Phys.* **2003**, *101*, 2083–2094.

[10] a) G. Liang, V. K. Peterson, Z. Wu, S. Zhang, J. Hao, C. Z. Lu, C. H. Chuang, J. F. Lee, J. Liu, G. Leniec, S. M. Kaczmarek, A. M. D'Angelo, B. Johannessen, L. Thomsen, W. K. Pang, Z. Guo, *Adv. Mater.* **2021**, *33*, 2101413; b) G. Liang, Z. Wu, C. Didier, W. Zhang, J. Cuan, B. Li, K.-Y. Ko, P.-Y. Hung, C.-Z. Lu, Y. Chen, G. Leniec, S. M. Kaczmarek, B. Johannessen, L. Thomsen, V. K. Peterson, W. K. Pang, Z. Guo, *Angew. Chem.*

Int. Ed. **2020**, *59*, 10594–10602; *Angew. Chem.* **2020**, *132*, 10681–10689.

[11] The Materials Project. Materials Data on Ge_2O_3 by Materials Project. United States. DOI: https://doi.org/10.17188/1316393.

[12] M. Lin, L. Ben, Y. Sun, H. Wang, Z. Yang, L. Gu, X. Yu, X.-Q. Yang, H. Zhao, R. Yu, M. Armand, X. Huang, *Chem. Mater.* **2014**, *27*, 292–303.

[13] a) J.-Y. Piao, Y.-G. Sun, S.-Y. Duan, A.-M. Cao, X.-L. Wang, R.-J. Xiao, X.-Q. Yu, Y. Gong, L. Gu, Y. Li, Z.-J. Liu, Z.-Q. Peng, R.-M. Qiao, W.-L. Yang, X.-Q. Yang, J. B. Goodenough, L.-J. Wan, *Chem* **2018**, *4*, 1685–1695; b) B. Xiao, H. Liu, J. Liu, Q. Sun, B. Wang, K. Kaliyappan, Y. Zhao, M. N. Banis, Y. Liu, R. Li, T. K. Sham, G. A. Botton, M. Cai, X. Sun, *Adv. Mater.* **2017**, *29*, 1703764.

[14] a) L. Zhao, H. Liu, X. Wang, Y. Wang, S. Wang, *Nanomaterials* **2019**, *9*, 697; b) Z. Zhao, J. Zhang, X. Wang, S. Wei, C. Zhao, W. Wang, *Chin. Phys. B* **2017**, *26*, 108201; c) F. Gao, M. A. Green, G. Conibeer, E. C. Cho, Y. Huang, I. Pere-Wurfl, C. Flynn, *Nanotechnology* **2008**, *19*, 455611.

[15] a) Y. Koyama, H. Arai, I. Tanaka, Y. Uchimoto, Z. Ogumi, *Chem. Mater.* **2012**, *24*, 3886–3894; b) M. M. Rahman, W. Y. Chen, L. Mu, Z. Xu, Z. Xiao, M. Li, X. M. Bai, F. Lin, *Nat. Commun.* **2020**, *11*, 4548; c) J. M. Clark, P. Barpanda, A. Yamada, M. S. Islam, *J. Mater. Chem. A* **2014**, *2*, 11807–11812.

[16] T. L. Cottrell, *The Strengths of Chemical Bonds*, Butterworths Scientific Publications, London, **1958**.

[17] H. Ryoo, S.-G. Lee, J.-G. Kim, S.-Y. Chung, *Adv. Funct. Mater.* **2019**, *29*, 1805972.

[18] a) M. Kuenzel, G.-T. Kim, M. Zarrabeitia, S. D. Lin, A. R. Schuer, D. Geiger, U. Kaiser, D. Bresser, S. Passerini, *Mater. Today* **2020**, *39*, 127–136; b) H. Liu, J. Wang, X. Zhang, D. Zhou, X. Qi, B. Qiu, J. Fang, R. Kloepsch, G. Schumacher, Z. Liu, J. Li, *ACS Appl. Mater. Interfaces* **2016**, *8*, 4661–4675; c) C. Yin, H. Zhou, Z. Yang, J. Li, *ACS Appl. Mater. Interfaces* **2018**, *10*, 13625–13634.

[19] a) F. M. de Groot, M. Grioni, J. C. Fuggle, J. Ghijsen, G. A. Sawatzky, H. Petersen, *Phys. Rev. B* **1989**, *40*, 5715–5723; b) F. Frati, M. Hunault, F. M. F. de Groot, *Chem. Rev.* **2020**, *120*, 4056–4110.

[20] Q. Li, Y. Wang, X. Wang, X. Sun, J. N. Zhang, X. Yu, H. Li, *ACS Appl. Mater. Interfaces* **2020**, *12*, 2319–2326.

[21] B. Xiao, J. Liu, Q. Sun, B. Wang, M. N. Banis, D. Zhao, Z. Wang, R. Li, X. Cui, T. K. Sham, X. Sun, *Adv. Sci.* **2015**, *2*, 1500022.

[22] K. Ariyoshi, Y. Iwakoshi, N. Nakayama, T. Ohzuku, *J. Electrochem. Soc.* **2004**, *151*, A296–A303.

[23] A. Singer, A. Ulvestad, H.-M. Cho, J. W. Kim, J. r Maser, R. Harder, Y. S. Meng, O. G. Shpyrko, *Nano Lett.* **2014**, *14*, 5295–5300.